The Planetary Science Journal, 3:192 (11pp), 2022 August https://doi.org/10.3847/PSJ/ac82ab

Dione's Thermal Inertia and Bolometric Bond Albedo Derived from Cassini/CIRS Observations of Solar Eclipse Ingress

Carly J. A. Howett and John R. Spencer

Southwest Research Institute, 1050 Walnut Street, Suite 300, Boulder, CO 80302, USA; howett@boulder.swri.edu

Received 2022 May 25; revised 2022 July 4; accepted 2022 July 14; published 2022 August 16

Abstract

On 2010 May 18 Cassini's Composite Infrared Spectrometer (CIRS) observed Dione's leading hemisphere as its surface went into solar eclipse. Surface temperatures derived from each of CIRS' focal plane 3 (FP3, $600-1100\,\mathrm{cm}^{-1}$) show a rapid decrease in Dione's surface temperature upon eclipse ingress. This change was compared to the model surface emission to constrain bolometric Bond albedo and thermal inertia. Seven FP3 detectors were able to constrain the observed surface's thermophysical properties. The bolometric Bond albedo derived from these detectors are consistent with one another (0.54 ± 0.05 to 0.62 ± 0.03) and that of diurnal studies (e.g., 0.49 ± 0.11, Howett et al. 2014). This indicates that Dione's albedo is uniform to within the uncertainties across the observed region of its leading hemisphere. The derived thermal inertias are consistent across detectors, $9 \pm 4\,\mathrm{J\,m^{-2}\,K^{-1}\,s^{-1/2}}$ (MKS) to 16 ± 8 MKS, and with previous diurnal studies (e.g., 8 to 12 MKS, Howett et al. 2014). The skin depth probed by the eclipse thermal wave is ∼0.6–1 mm, which is much shallower than that probed by diurnal cycles (∼50 mm). Thus, the agreement in thermal inertia between the eclipse and diurnal studies indicates that Dione's subsurface structure is uniform from submillimeter to subcentimeter depths. This is different from the Jovian system, where eclipse-derived thermal inertias are much lower than those derived from diurnal studies. The cause of this difference is not known, but one possibility is that the E-ring grains that bombard Dione's leading hemisphere overturn it, causing uniformity to centimeter depths.

Unified Astronomy Thesaurus concepts: Saturnian satellites (1427); Natural satellite surfaces (2208); Surface ices (2117)

1. Introduction

Observing a surface's thermal response to an eclipse is useful because it provides an insight into the structure of the uppermost surface (submillimeter), which is shallower than the millimeter depths of diurnal studies and centimeter depths of seasonal studies (see below for a more detailed discussion of skin depth). However, there are few such studies for Saturn's icy satellites because of the difficulty in making the required observations from the ground, but some do exist. For example, Neugebauer et al. (2005) used observations taken at the Palomar observatory in 1978 January at 20 μm to observe Iapetus entering a solar eclipse caused by Saturn's rings. The eclipse lasted ∼1 hr and sampled the top ∼0.4 mm of the surface. The results showed that Iapetus had a thermal inertia of <10 MKS, which is very low by comparison to icy satellites in the Jovian system (see below, or references within Howett et al. 2010; Ferrari 2018). Hanel et al. (1981) observed Rhea in eclipse with Voyager 1's Infrared Interferometer Spectrometer (IRIS; see Hanel et al. 1980). Their results indicated a high and low thermal inertia component on Rhea's surface, where the high thermal inertia was believed to be a solid material with a block size at least that of the thermal skin depth (∼10 cm), while the low thermal inertia component was predicted to be a thin frosty layer. Pearl et al. (2008) presented the cooling curves of an eclipse of Dione that occurred on 2008 March 28 as derived from Cassini's Composite Infrared Spectrometer (CIRS), but the results were not published in detail.

Studies of eclipse observations of Jupiter's satellites are more plentiful and typically show that these satellites have a lower thermal inertia than that inferred from diurnal studies. For example, on Europa the eclipse-derived thermal inertia is 14 ± 5 MKS compared to between 45 and 150 MKS for the diurnal value (see Hansen 1973; Spencer 1999; Rathbun et al. 2010). For Ganymede (Callisto) the eclipse-derived thermal inertias are 14 ± 3 MKS (10 ± 1 MKS), compared to diurnal values of 70 ± 20 MKS (50 ± 10 MKS) (Morrison & Cruikshank 1973; Spencer 1987). This implies that the thermal inertia on the Jovian icy satellites increases with depth, perhaps because compaction decreases the surface porosity with increasing depth.

To be consistent with the literature, we refer to the albedo derived from surface temperatures as the bolometric Bond albedo. However, it should more precisely be called the hemispherical albedo (Hapke 1993), as Bond albedo refers to the entire surface. See Young (2017) for a more detailed explanation of albedo.

The thermal inertia and bolometric Bond albedo of Dione's surface have been derived from studies that use diurnal temperature variations (e.g., Howett et al. 2010, 2014). Howett et al. (2014) mapped Dione's albedo and thermal inertia, showing that Dione's thermal inertia is low, 8–11 MKS, with the highest values on its leading hemisphere. The thermal inertia increase on the leading side is believed to be due to surface modification by high-energy electrons that preferentially bombard Dione's equatorial leading hemisphere (see Hamilton & Burns 1994; Paranicas et al. 2014; Nordheim et al. 2017). These electrons then mobilize water molecules in the surface, which increases the contacts between grains and hence the bulk thermal conductivity (Howett et al. 2011; Schenk et al. 2011; Schaible et al. 2017).

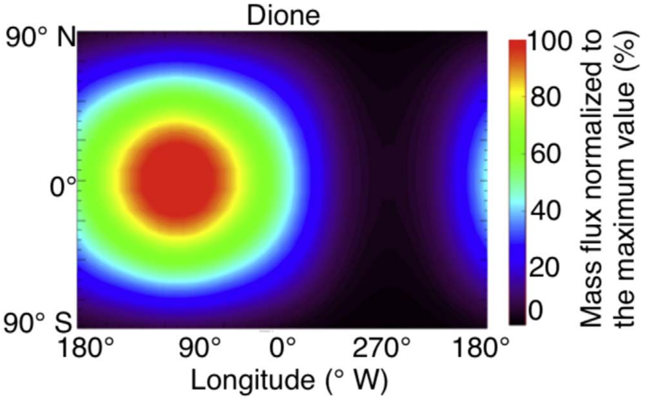

Figure 1. The mass influx of E-ring grains onto Dione, where the flux has been normalized to its maximum value (from Kempf et al. 2018).

Dione's disk-integrated bolometric Bond albedo was found to be 0.44 ± 0.13 by Howett et al. (2014), which is consistent with other studies in the literature, e.g., 0.52 ± 0.08 (Pitman et al. 2010) and 0.63 ± 0.15 (Howett et al. 2010). Howett et al. (2014) also confirmed that Dione's trailing hemisphere is darker than its leading side (0.39 ± 0.13 compared to 0.49 ± 0.11; e.g., Buratti & Veverka 1984: Burratti et al. 1990; Schenk et al. 2011; Filacchione et al. 2018). This albedo variation is believed to be due to the preferential bombardment of Dione's leading hemisphere by E-ring grain particles (Figure 1; Hamilton & Burns 1994; Kempf et al. 2018), which plausibly cause surface brightening (Verbiscer et al. 2007; Stephan et al. 2010; Sciponi et al. 2013).

The depth a thermal wave propagates through an icy satellite surface will depend on the nature of the surface and timescale of insolation variations it receives. Specifically, thermal wave penetration depth is defined by the thermal skin depth (δ). Diurnal skin depth is mathematically described as $\delta = \Gamma/\rho C_p\sqrt{\omega}$, where Γ is thermal inertia (in units J m^{-2} K^{-1} $s^{-1/2}$, henceforth referred to as MKS), ρ is density, C_p is specific heat capacity, and ω is angular velocity of rotation. Thermal inertia describes how well a surface is able to store and release thermal energy; it is mathematically described as $\sqrt{k\rho_0(1-p)C_p}$, where ρ_0 is the zero-porosity density, p is the porosity, and k is the thermal conductivity. ω *is equal to* $2\pi/T$, where T is the timescale being considered (e.g., for diurnal studies it is the target's rotation period). So targets with longer rotation periods (i.e., smaller ω) will have larger skin depths. The same principle can be extended to different insolation variation timescales; eclipse observations (which typically last about a few hours, and thus adopt this time as their T value) have very shallow skin depths, whereas diurnal cycles will have deeper ones, and finally seasonal cycles (where T is now the length of the target's year) will have deeper ones still.

The exact depths reached by these cycles will also depend on the thermal inertia, density, and specific heat of the surface. Typically in the outer solar system the thermal inertias of icy satellites vary from a few to tens of MKS (e.g., Howett et al. 2010). For example, on Rhea thermal inertias between 1 and 46 MKS were determined to provide an adequate fit to seasonal temperature variations (Howett et al. 2016), while 8^{+12}_{-5} MKS and 9^{+9}_{-5} MKS fitted the diurnal temperatures on the trailing and leading hemisphere, respectively (Howett et al. 2010). Assuming a thermal inertia of 8 MKS, a surface density of nonporous ice of 0.924 g cm^{-3}, a specific heat of water ice at 90 K of 0.8 J K^{-1} g^{-1} (Spencer & Moore 1992), and a porosity of 0.5, the diurnal and seasonal skin depths of Rhea were shown to be 0.5 and 26 cm, respectively (Howett et al. 2016). Assuming the same thermal inertia (8 MKS) and a 1 hr eclipse (i.e., assuming that ω is $2\pi/60^2$), Rhea's eclipse skin depth is 0.05 cm. So eclipse observations provide an opportunity to probe the very top layers of the surface.

Table 1

Details of the Eclipse Observed on 2010 May 18

Observation Details	Result
Penumbra eclipse start time (UTC)	03:02:55
Umbra eclipse start time (UTC)	03:03:39
Penumbra eclipse start time (UTC)	05:55:54
Penumbra eclipse end time (UTC)	05:56:27
Cassini orbit (revolution)	131
Spacecraft−Dione distance (km)	209,823 to 219,132
Subspacecraft longitude (deg W)	53.7 to 58.3
Subspacecraft latitude (deg)	0.0
Subsolar longitude (deg W)	352.2 to 355.5
Subsolar latitude (deg N)	4.3
Phase (deg) at subspacecraft location	58.6 to 66.5
Dione−Sun distance (au)	9.52

Note. Timing is given at the subsolar point on Dione.

Here we analyze a single CIRS observation of an eclipse ingress on Dione, with the aim of using the cooling curve to constrain Dione's thermal inertia and albedo. By comparing this result to the previously published thermal inertias derived from diurnal studies, we will constrain the structure of Dione's surface and determine whether Dione's thermal inertia follows the same trend as the Jovian icy satellites (i.e., increasing with depth) or not.

2. Introduction to Cassini's Composite Infrared Spectrometer

This work focuses on observations made by the CIRS on board the Cassini spacecraft (Flasar et al. 2004). CIRS was a Fourier Transform Spectrometer (FTS) with two interferometers that shared a single scan mechanism and telescope. CIRS has three focal planes: focal plane 1 (10–600 cm^{-1}, 16.7–1000 μm), focal plane 3 (FP3, 600–1100 cm^{-1}, 9.1–16.7 μm), and focal plane 4 (1100–1400 cm^{-1}, 7.1–9.1 μm). FP3 had a row of 10 detectors, each of which had a 0.273 by 0.273 mrad field of view (FOV). The results we analyze here were taken by FP3 of Dione's sunlit hemisphere as it went into eclipse (see Table 1) in "blink mode" (i.e., odd and even detector readouts are switched between). Thus, for reasons outlined in Nixon et al. (2009, 2019), the FP3 detectors are numbered 11–20 in this observation.

3. Data and Analysis

On 2010 May 18 Saturn blocked the Sun from reaching Dione, causing Dione's sunlit leading hemisphere to experience a solar eclipse. The exact eclipse onset time depends upon where on the surface of Dione you are located. We used the standard NAIF/SPICE routine gfoclt and files sat450.bsp and

Table 2
The Longitude, Latitude, Emission Angle Ranges, and Eclipse Ingress Covered by the Fields of View of Each CIRS Detector

CIRS FP3 Detector Number	Longitude Range of the FOV (deg W)	Latitude Range of the FOV (deg N)	Emission Angle Range of Entire FOV (deg)	Emission Angle Range of Center of FOV (deg)	Predicted Eclipse Start Time (UTC)
11	46–58	21–33	23–33	26–28	03:02:50
12	39–52	18–30	21–30	24–28	03:02:50
13	33–45	15–26	21–30	25–28	03:02:51
14	26–39	12–23	22–32	26–32	03:02:52
15	20–33	9–20	25–36	30–35	03:02:54
16	12–27	6–16	30–42	35–41	03:02:57
17	5–20	3–13	36–49	42–47	03:03:01
18	353–13	−0–10	44–58	49–56	03:03:07
19	333–4	−3–7	52–71	59–67	03:03:10
20	324–354	−7–4	64–90	73–90	03:03:27

Note. The range of emission angles is also given at the center of the FOV. As per the text, the pointing knowledge of CIRS FP3 is predicted to be ∼10% of the FOV, which translates to an estimated uncertainty in the emission angle of <1° for all detectors, except for detectors 19 and 20, where it increases to <2° owing to the larger size of the FOV toward the limb.

de440.bsp to determine the eclipse onset time for its default location: target center. Noting that an observer at Dione's subsolar point and its center will experience the same timing of the eclipse, we could use this routine to derive the eclipse timing. The times determined from this analysis are given in Table 2. As the table shows, the subsolar point on Dione eclipse onset lasts ∼42 s starting at 03:02:50 UTC, equivalent to the subsolar eclipse time if the Sun was a point source, as assumed in the thermal model. We then use a Planetary Data System (PDS) tool (Saturn View 3.0; Showalter 1995) to produce simulated images of this eclipse as seen from Cassini to determine when, relative to this mid-time, each of the detectors would experience the eclipse (Table 2).

We note that this technique ignores any effects Saturn's atmosphere would have on the eclipse timing. As the results show (Table 2), all the detectors experience an eclipse onset midpoint within 30 s of 03:02:55 UTC, with most (detectors 11–17) within 10 s. Since the computational overhead of modeling is high and eclipse onset is rapid, we assume a single eclipse onset time for all detectors (i.e., in our model we assume that the sunlight drops to zero at 03:02:55 UTC).

The details of the observation are given in Table 1. All 10 of CIRS' FP3 detectors stared at Dione from 02:52:37 until 03:29:11 UTC (i.e., during ingress only). The footprints of each observation (as given by the reconstructed CIRS pointing files) for each detector are shown in Figure 2 and detailed in Table 2. The biggest source of uncertainty in the pointing is from spacecraft attitude estimation errors, which are estimated to be 0.027 mrad in X-axis and 0.01 mrad in the Z-axis (Pilinski & Lee 2009). The CIRS instrument is aligned with the spacecraft Y-axis, the 10 FP3 detectors are aligned along the Z-axis (typically the across-track direction when scanning), and the X-axis describes their width (typically in the along-track direction); see discussion in Nixon et al. (2019) for more details of the CIRS detector orientation. Each CIRS FP3 detector footprint is 0.273 mrad, so the pointing accuracy is about 10% of the size of one CIRS detector FOV.

As Figures 2 and 3 show, the stare observation was very stable (very little change in the location of the footprints during the observation) and stretched over Dione's leading hemisphere through the subsolar point. The lower numbered detectors cross the large Aeneas crater, while the higher numbers cover brighter terrain with smaller craters (Figure 3). The higher-number detectors are closer to the subsolar point (shown in Figure 2 as a diamond) and are thus expected to be observing warmer surface temperatures. Table 2 also gives the emission angles for each FP3 detector, which shows that the emission angle increases with detector number. So while the higher detector numbers are expected to have a higher signal-to-noise ratio (due to the warmer scenes they are observing), their results have to be treated with caution since thermal data taken at high emission angles (near the limb) are difficult to interpret accurately. This is because at high emission angles the surface is being viewed "side on", which means that topographic highs and slopes facing the spacecraft will be preferentially observed (e.g., crater rims). The thermal emission of these regions is typically not representative of the total emission from the surface (i.e., from both topographic highs and lows).

Each CIRS FP3 observation produces a single spectrum, which was converted to temperature by finding the closest blackbody fit. The surface temperature was determined by fitting a blackbody curve to the observed emission using the downhill simplex method (see Nelder & Mead 1965) in IDL's amoeba algorithm, on the assumption that the surface emits as a blackbody. The measurement noise on a single spectrum is assumed to be the standard deviation of the difference between the observed spectrum and its best-fitting blackbody curve. The noise on the determined surface temperatures is derived using a two-step Monte Carlo technique: First, synthetic noise with a comparable magnitude to the measurement noise is created and added to the previously determined best-fitting blackbody curve. Then, this spectrum is fitted by a blackbody emission spectrum using the same fitting technique. This process is repeated numerous times, and the surface temperatures that are able to fit the data within the predetermined noise are binned into a histogram. By assuming a normal distribution we can also assume that one standard deviation covers 34.1% of values above and below the mean. Thus, we can use these results to derive nonsymmetrical temperature uncertainties. The results are shown in Figure 4, which shows the change in Dione's surface temperature as a function of time from the start of the eclipse. As the figure shows, the surface temperatures in all detectors are stable until eclipse onset, after which time they gradually decrease.

To determine which thermal inertia and albedo values are able to reproduce the CIRS-derived surface temperatures, the observed and modeled temperatures are compared. We use the 1D thermal model *thermprojrs* (see Spencer 1989), which calculates, in one dimension, the subsurface conductive heat flow to determine the temperature as a function of depth and time of day. The lower boundary is set to a depth at which there is negligible temperature change with the diurnal temperature cycle. The upper boundary is set so that the thermal radiation and incident solar radiation are balanced with the heat

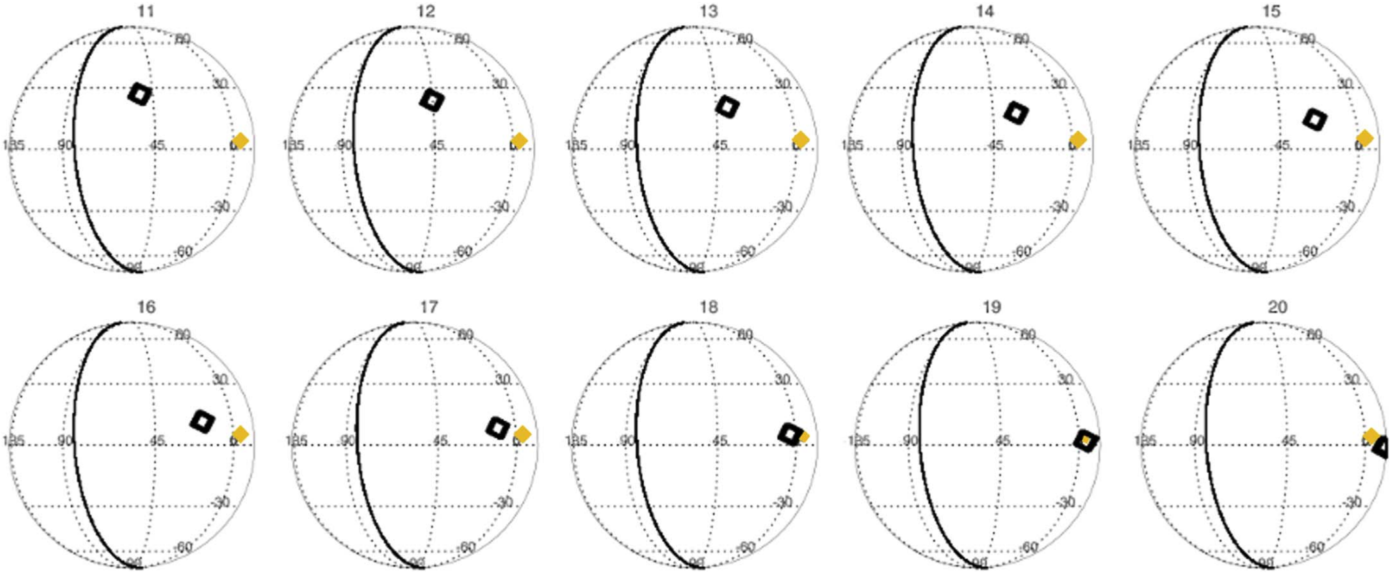

Figure 2. The view of Dione from Cassini during the eclipse observation. The black open squares show the footprint of each FP3 observation for each detector during the observation. Longitudes are shown in °W. The day/night terminator is shown as a solid black line with the night side on the left, and the yellow solid diamond indicates the subsolar position (352.2° W to 355.5° W, 4.3° N). The images are centered on the mean subspacecraft position (55.9° W, 0.0° N). The number of the FP3 detector whose position is plotted is given at the top of each map.

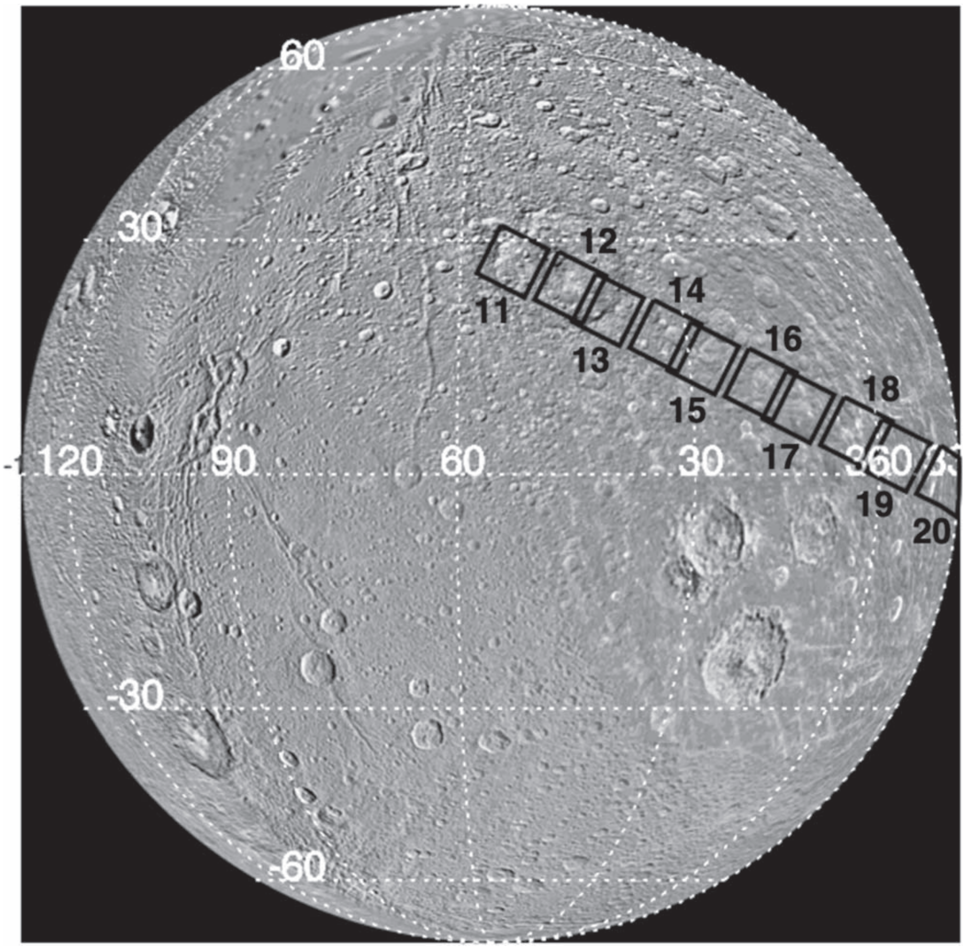

Figure 3. The footprint of all 10 FP3 detectors are overplotted during the eclipse observation onto a map of Dione (PIA08413). The latitude and western longitudes (in degrees) are given in white lettering, while the detector numbers are given in black. The footprints are taken at the midpoint of the observation (03:11:04 for odd detectors, 03:10:59 for even ones). Following Figure 2, the image is centered on the mean subspacecraft position (55.9° W, 0.0° N). The detector numbers increase from left to right (see Figure 2 for details).

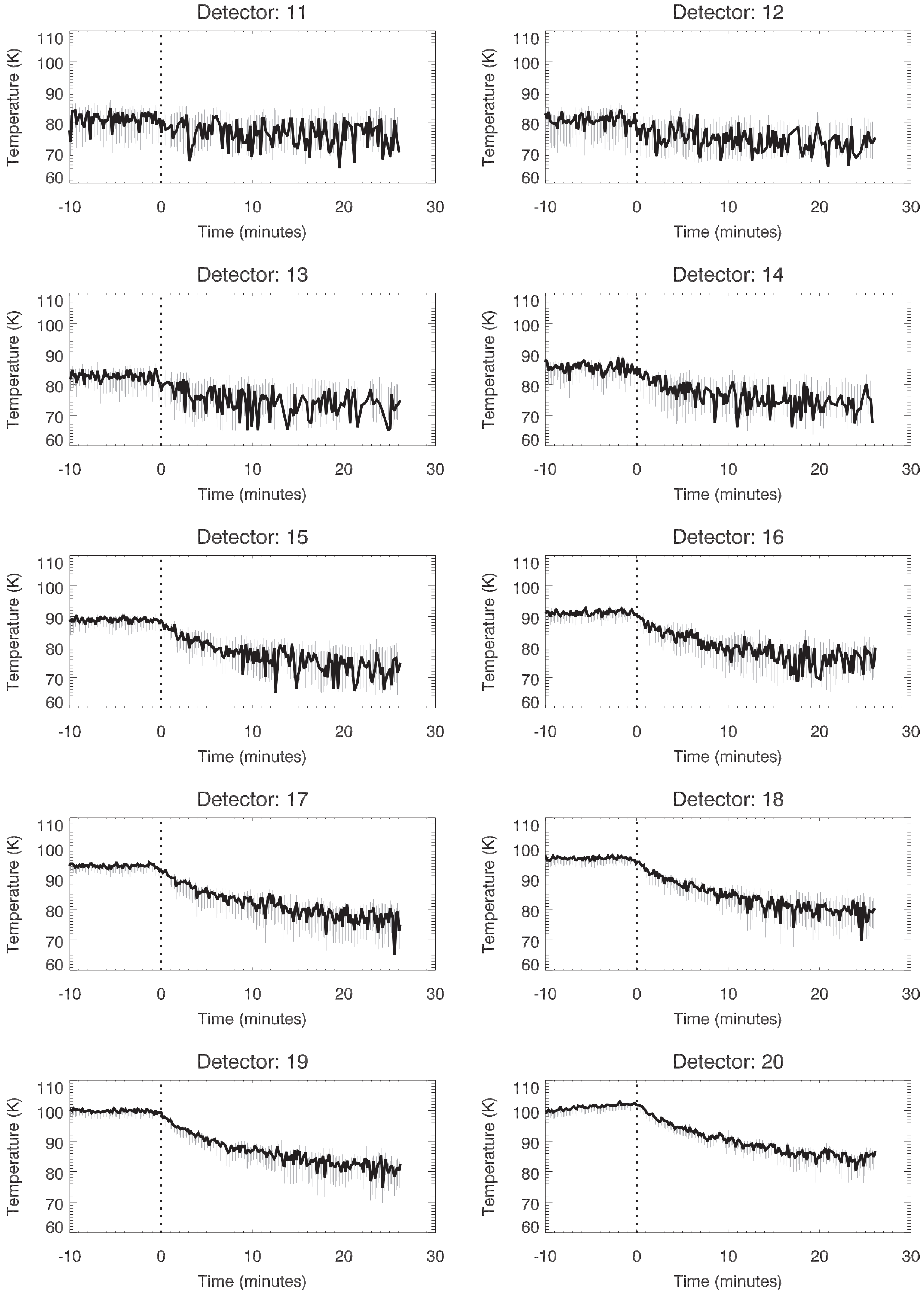

Figure 4. The CIRS-derived blackbody temperature change with time for each detector relative to eclipse ingress on 2010 May 18 03:02:55 UTC. The error on each derived temperature is shown by the light-gray error bars.

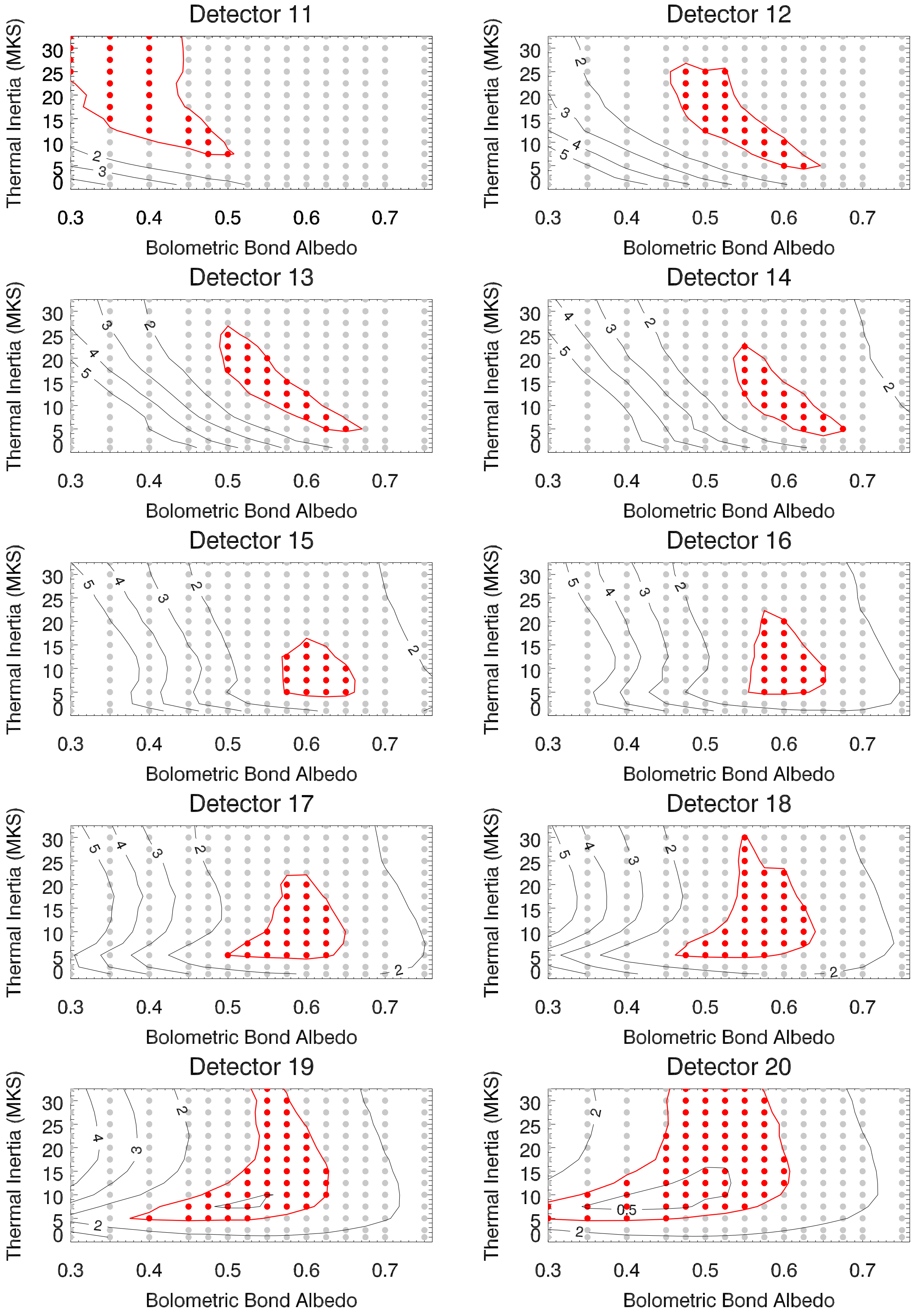

Figure 5. Reduced χ^2 of each FP3 detector; the contours are shown at 0.1, 0.2, 0.3, 0.4, 0.5, 1.0, 2, 3, 4, 5, and 10. The contour at unity is shown in red, since inside of this contour is when the modeled albedo and thermal inertia values are able to reproduce the observed radiances. The albedo and thermal inertias modeled are shown by the circles, with those in red highlighting the thermophysical parameters that produce a reduced $\chi^2 \leqslant 1$.

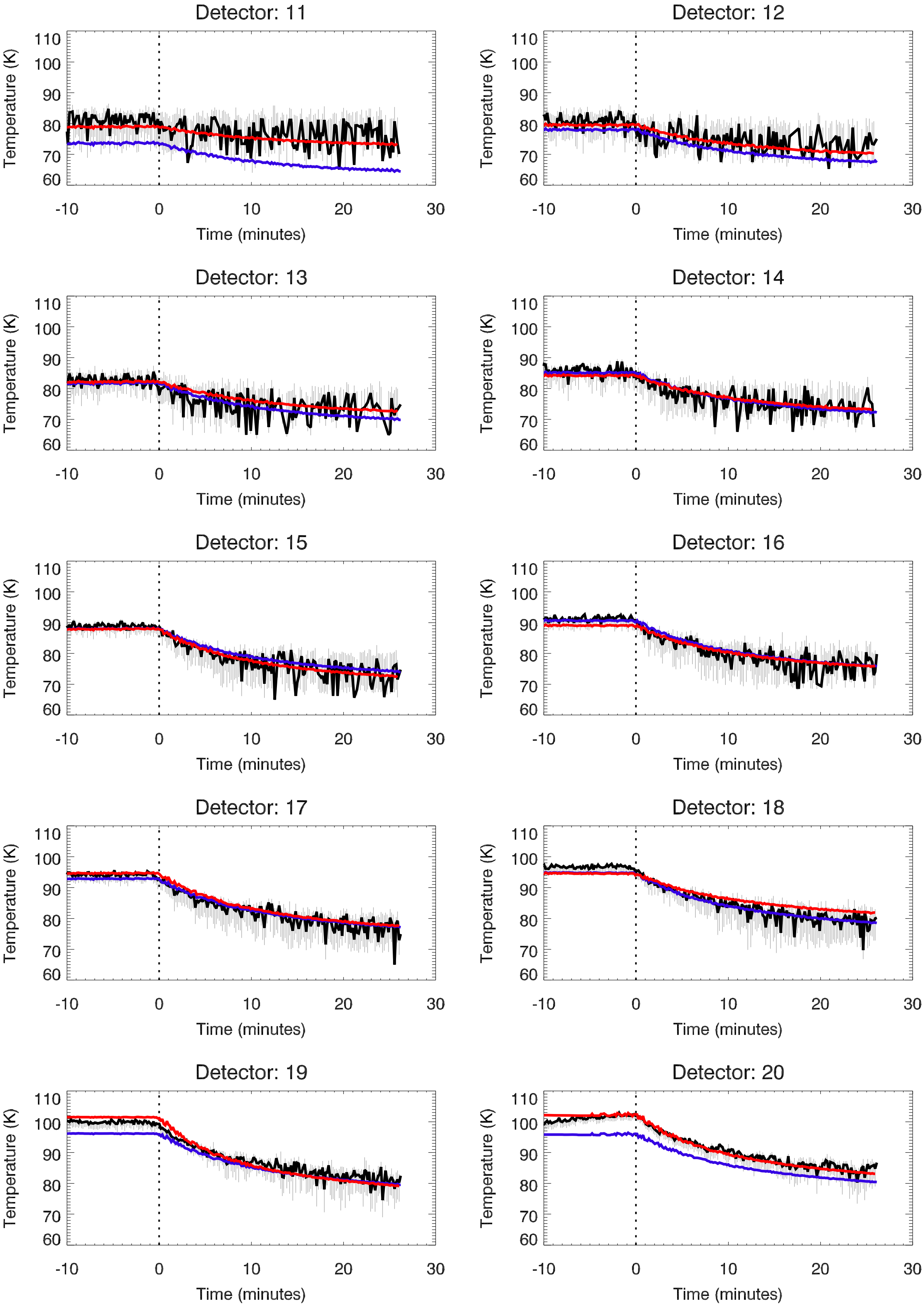

Figure 6. The change in surface temperature derived from Cassini CIRS observations (see Figure 3) is compared to those predicted by every detector's mean albedo and thermal inertia model (red) and a model with an albedo of 0.60 and a thermal inertia of 10 MKS (purple). These values were chosen because they could provide an adequate fit for detectors 12–18 (see text and Figure 5 for details). The gray lines indicate the error on the derived surface temperatures.

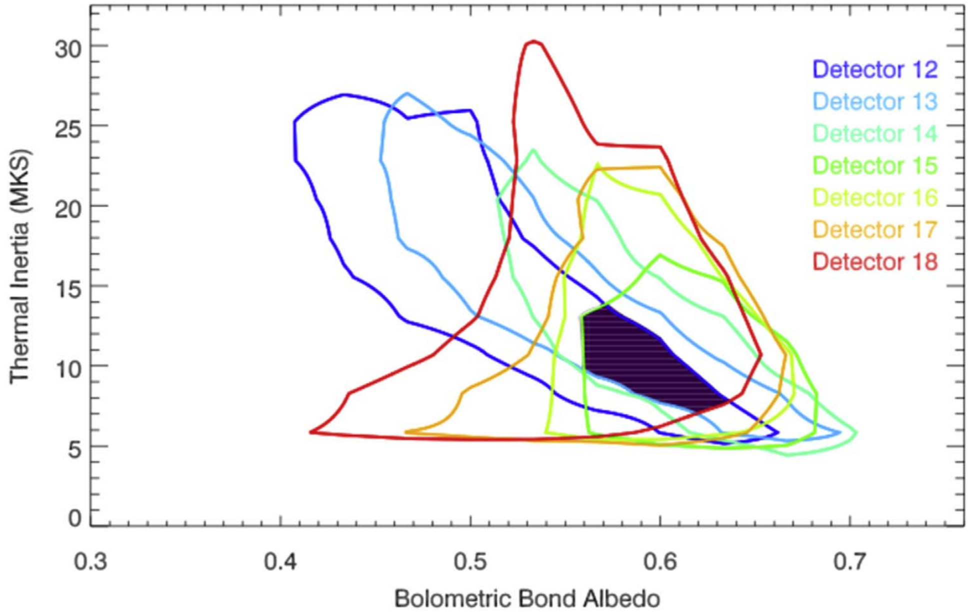

Figure 7. The reduced χ^2 curves from Figure 4 at unity for detectors 12–18. The results have been interpolated to increments of 0.001 in albedo and 0.05 in thermal inertia over the original ranges to allow the overlapping regions to be better sampled. The shaded region shows the thermal inertia and albedo values that have a reduced χ^2 of $\leqslant 1$ for all detectors. It covers albedos between 0.56 and 0.63 and thermal inertias between 7 and 14 MKS (rounded to the nearest two decimal places and integer value, respectively). The results show that some thermal inertia and albedos are able to fit all observations, so it is feasible that the surface is uniform across the area observed. However, it is also possible that the regions observed have widely different thermophysical properties (i.e., the regions outside the shading).

conducted to and from the surface and the change in the heat content of the surface layer. The specific geometry of the observations is used: Dione's rotation speed, its heliocentric distance and subsolar position during the observations, and the latitude/local times of the observations. The model determines surface temperatures during a full Saturn year, accounting for both seasonal variations in heliocentric distance and subsolar latitude, in addition to diurnal and eclipse insolation variations. The model assumes a unit emissivity and does not include either heating or reflected sunlight from Saturn. Bolometric Bond albedos between 0.3 and 0.8 were modeled. Across the full albedo range an increment of 0.05 was assumed, but between 0.475 and 0.675 the albedos were sampled at 0.025 increments to better constrain the fit. Thermal inertias of 1 MKS, and then between 2.5 and 32.5 MKS, were modeled in increments of 2.5 MKS. These were chosen to cover the albedo and thermal inertia range determined for Dione by previous studies (e.g., Howett et al. 2010, 2014).

A surface with a higher albedo is able to better reflect the incoming solar radiation and thus displays a lower daytime surface temperature. In these observations a higher albedo surface would result in a lower baseline (starting) temperature. Surfaces with a higher thermal inertia respond slower to a change in insolation than lower thermal inertia ones, due to a better conductivity between the grains. Thus, surface temperature would decrease more slowly upon eclipse ingress for a higher thermal inertia surface than a lower thermal inertia one. Since albedo and thermal inertia variations manifest differently in the resulting cooling curves, it is possible to differentiate between them.

The quality of fit between the data and model is tested using the reduced χ^2 statistic; specifically, it tests how well the observed FP3 spectrum is fitted by a surface emitting at the blackbody temperature predicted by the model (for a given albedo and thermal inertia value). In this calculation we assume that the error at a given wavelength for a single spectrum is the absolute difference between the observed spectrum and its best-fitting blackbody temperature spectrum. An albedo and thermal inertia combination are assumed to be consistent with the data if the reduced χ^2 is unity or lower. The results are shown in Figure 5, for the data from each FP3 detector. As the figure shows, reduced χ^2 contours of unity are reached, but not notably lower than that—implying that the noise estimates are appropriate (i.e., not so relaxed that they do not offer any constraint).

4. Discussion

Figure 4 shows the temperatures derived from the CIRS observations. Detector 11 has uncertainties that are the same magnitude as surface temperature change. As previously discussed, this is because it is viewing the scene farthest from the subsolar point, which is thus cooler and therefore has a lower radiance than the other scenes. This large error makes it impossible to accurately constrain the thermal inertia and albedo, though lower limits to albedo and lower limits to thermal inertia can be obtained (Figure 5). Table 2 provides the emission angles of the detectors and shows that detectors 19–20 have emission angles much higher than 60°. This high emission angle makes the thermal emission difficult to interpret, due to surface roughness effects as discussed above. So detectors 12–18 lie in the sweet spot: close enough to the subsolar point that their surface emission has high signal-to-noise ratio (and thus the surface temperatures derived from it have low uncertainties), but they are taken at low- to mid-range emission angles. This is evident in Figure 5, where the region of parameter space bounded by a reduced χ^2 value of unity strongly constrains albedo and thermal inertia.

To determine the best-fitting thermophysical properties for each detector, we find the mean and standard deviation of all of the modeled values of thermal inertia and albedo with reduced $\chi^2 < 1$. This produces a weighted estimate of the

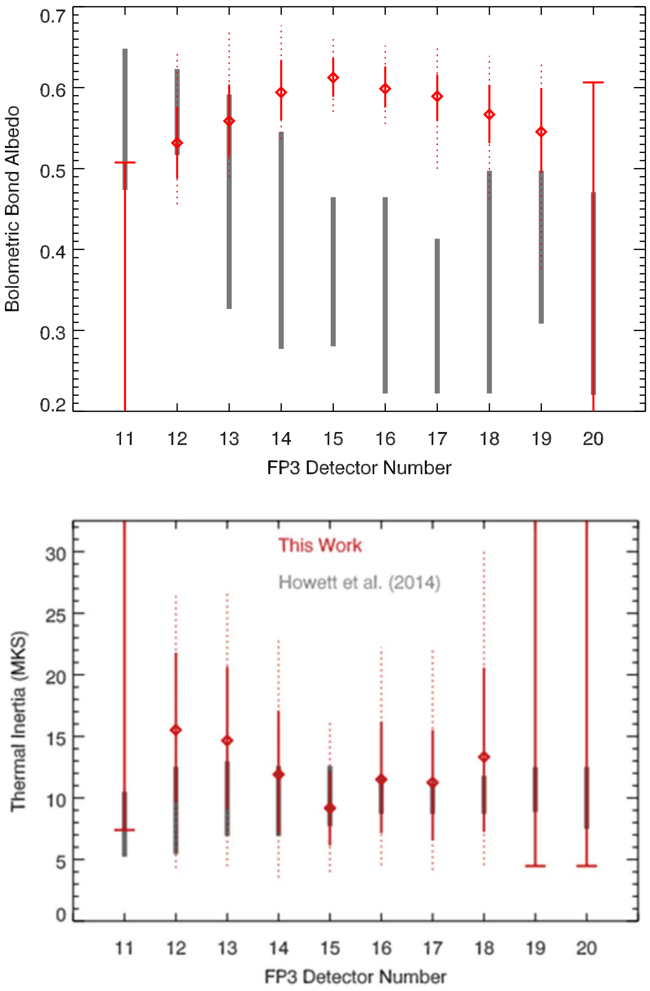

Figure 8. The red solid line shows the mean and standard deviation of bolometric Bond albedo and thermal inertia with FP3 detector number derived in this work. The red dotted lines show the total extent of the thermophysical properties derived. The gray lines show the results derived in a previous study of the same regions, which used diurnal variations (Howett et al. 2014).

thermophysical properties for the location observed by each detector. For example, an albedo that is able to fit the observed data with multiple thermal inertia values will be more strongly weighted than one that can fit the data with only a single thermal inertia. The change in surface temperature predicted by the mean albedo and thermal inertia is compared to the observed surface temperature in Figure 6. As the figure shows, the model temperatures agree with the temperatures observed within their uncertainty, as expected.

Figure 7 compares the location of the reduced χ^2 unity contours for detectors 12–18, which lie in the "sweet spot." The figure shows that albedos between 0.56 and 0.63 with thermal inertias between 7 and 14 MKS are able to adequately fit the data for all these detectors. Thus, there is no statistically meaningful variation detected in the thermophysical properties across the detector locations. As a check to this result, the surface temperatures predicted by a model with a thermal inertia of 10 MKS and an albedo of 0.60 are also compared to the derived surface temperatures in Figure 6. As this figure shows, such a model does not always reproduce temperatures as close to those derived as the best-fit model, but it generally follows the observed change in temperatures and fits them within their uncertainty, providing support that a single albedo–thermal inertia pair adequately reproduces the derived surface temperatures.

Figure 8 compares the results to one another and also to previous studies that derive these values for Dione from CIRS observations of diurnal variations in thermal emission (see Howett et al. 2014). The figure shows that both the bolometric Bond albedo and thermal inertia generally agree, following the well-documented trend of albedos on Dione's leading hemisphere decreasing toward its Saturn-facing one (e.g., Buratti et al. 1990; Howett et al. 2014; Schenk et al. 2011; Filacchione et al. 2018). This change is thought to be due to E-ring bombardment of the leading hemisphere (Verbiscer et al. 2007; Schenk et al. 2011). However, the derived albedos for detectors 15–17 (which cover 5° to 33° W, 3° to 20° N) are notably higher than previous results. The albedos from detectors 15–17 remain ~flat (within their uncertainty), instead of decreasing as expected by the typical trend. This could be due to these detectors partially covering bright wispy terrain (Figure 3), but the full reason is not known.

As previously discussed, a small increase in thermal inertia was discovered at low latitudes on Dione's leading hemisphere compared to its background value (11 MKS, compared to 8 MKS; see Howett et al. 2014). Similarly located but stronger anomalously high thermal inertias have also been discovered on Mimas (Howett et al. 2011, 2020) and Tethys (Howett et al. 2012, 2019). In these anomalies the thermal inertia is highest toward the center of the leading hemisphere. In our thermal inertia results such variations (~3 MKS) are too small to be seen, as thermal inertias between 8 and 13 MKS fit all of the eclipse results.

Assuming the same porosity, specific heat, and surface density as in Section 1 and a thermal inertia between 8 and 11 MKS derived from diurnal observations (Howett et al. 2014), the skin depth of the diurnal thermal wave on Dione is 41–57 mm. This is much higher than the skin depth of the eclipse thermal wave, which, as Table 3 shows, varies from 0.6 to 1.0 mm for the thermal inertias derived here. However, despite the different skin depths, the thermal inertias derived from both the eclipse and diurnal study are comparable (Figure 8). This implies that the surface structure of Dione does not vary greatly between the uppermost layer (submillimeter scale) and subsurface (subcentimeter scale). As outlined in Section 1, this is in contrast to the surface structure of the Jovian icy satellites derived from eclipse cooling curves, which appear to have increasing thermal inertia with depth.

The reason for Dione's apparent surface uniformity with depth is not known, but it could be the effect of E-ring grain bombardment. E-ring grains are expected to preferentially bombard Dione's leading hemisphere at high (>5 km s^{-1}) velocities (Figure 1; Hamilton & Burns 1994; Kempf et al. 2018; Verbiscer et al. 2007). The ejecta produced by this bombardment are expected to mostly fall back onto the surface (Verbiscer et al. 2007), perhaps creating the uniform surface structure we observe. A good test for this would be to determine the thermal inertia of Dione or Rhea's trailing hemisphere from eclipse measurements. Both of these regions are bombarded less by E-ring grains than Dione's leading hemisphere, and so if this hypothesis is correct, we would expect the eclipse-derived thermal inertias to have a lower value than those derived from diurnal temperature variations in these locations.

Table 3
The Mean and Uncertainty (Standard Deviation) of the Bolometric Bond Albedo and Thermal Inertia Constrained for Different FP3 Detector Observations, Assuming Both the Range of Originally Modeled Thermophysical Properties and the Interpolated Results

FP3 Detector Number	Weighted Mean Bolometric Bond Albedo and Standard Deviation	Weighted Mean Thermal Inertia and Standard Deviation (MKS)	Bolometric Bond Albedo Range	Thermal Inertia Range (MKS)	Thermal Skin Depth (cm)
11	⩽0.51	⩾7.3			>0.05
12	0.53 ± 0.04	15.5 ± 5.8	0.46–0.65	4.3–26.8	0.10 ± 0.04
13	0.56 ± 0.04	14.7 ± 5.6	0.49–0.67	4.5–26.8	0.09 ± 0.04
14	0.59 ± 0.03	11.9 ± 4.7	0.54–0.68	3.5–23.2	0.08 ± 0.03
15	0.61 ± 0.02	9.2 ± 3.0	0.57–0.66	4.0–16.4	0.06 ± 0.02
16	0.60 ± 0.02	11.5 ± 4.4	0.55–0.65	4.5–22.3	0.07 ± 0.03
17	0.59 ± 0.03	11.2 ± 4.7	0.50–0.65	4.2–22.1	0.07 ± 0.03
18	0.57 ± 0.04	13.3 ± 6.1	0.46–0.64	4.5–30.2	0.09 ± 0.05
19	0.55 ± 0.05	14.7 ± 7.5	0.38–0.63	⩾4.5	⩾0.03
20	⩽0.61	⩾4.5	0.30–0.61	4.5–32.5	⩾0.03

Note. Where thermal inertia is constrained, the thermal skin depth of the surface is also provided using the mean and standard deviation thermal inertia derived from the originally modeled properties. See main text for more details, including the assumed surface properties of the skin depth calculation.

Data that could assist with this comparison do exist. For example, on 2008 November 16 (Rev 93) CIRS made a slow FP3 scan of Dione's mid-northern latitudes on its Saturn-facing hemisphere. During this time, an eclipse occurred from 14:47:32 to 17:43:14 UTC. CIRS also stared at low to equatorial regions of Rhea's Saturn-facing hemisphere with FP3 on 2008 August 19 (Rev 81), while an eclipse occurred from 10:36:36 to 12:30:42 UTC. The analysis of these data sets is beyond the scope of this work and is instead left as a topic of follow-up studies.

5. Conclusion

Observations made by Cassini CIRS showed that the surface temperature of Dione cooled rapidly as it entered a solar eclipse. No statistically significant variation in bolometric Bond albedo or thermal inertia was detected across the different regions observed. However, we note that the albedos derived for detectors 15–17 are almost twice those previously determined and do not display the previously observed trend of decreasing toward the sub-Saturn point. The cause of this potential discrepancy is not understood. Since the new and previous studies used observations with different spatial resolutions, these albedo differences could be picking up variations in albedo on small spatial scales, or it could simply be noise. The mean and standard deviation of the bolometric Bond albedo values able to fit the data varied from 0.54 ± 0.05 to 0.62 ± 0.03. These results are in agreement with previously derived albedos for Dione's leading hemisphere, e.g., 0.49 ± 0.11 (Howett et al. 2014). Interestingly, the mean and standard deviation of thermal inertia values found by different detectors (9 ± 4 MKS to 16 ± 8 MKS) are consistent with those derived from diurnal temperature variations (8 to 11 MKS; Howett et al. 2014). This is surprising since the skin depth sampled by eclipse and diurnal temperature variations is different (submillimeter scale versus subcentimeter scale, respectively), so it implies that Dione's surface has a uniform structure between the uppermost and deeper surface layers. This is in contrast to icy satellites in the Jovian system, which have been shown to have a higher thermal inertia deeper in their surface (i.e., in diurnal studies) than derived for the uppermost surface from eclipse cooling. One possible explanation for Dione's uniformity is the bombardment by E-ring grains preferentially on its leading hemisphere (which is the one CIRS observed here). These impacts blast the surface, resulting in ejecta that predominantly fall back onto the surface, which could make it more uniform. Similar studies of Dione's trailing hemisphere or Rhea could test this hypothesis, since they are both bombarded less than Dione's leading hemisphere and thus may have a difference in surface properties with depth.

Thanks are due to the Cassini project and especially the CIRS team that made these data possible. We also thank Dr. Mark Showalter for his discussion of modeling the geometry of the eclipse onset and Drs. Georgina Miles and Julien Salmon for their helpful discussions. This work was supported by the Cassini Project, grant 80NSSC17M0061.

ORCID iDs

Carly J. A. Howett https://orcid.org/0000-0003-1869-4947
John R. Spencer https://orcid.org/0000-0003-4452-8109

References

Buratti, B., & Veverka, J. 1984, Icar, 58, 254
Buratti, B. J., Mosher, J. A., & Johnson, T. V. 1990, Icar, 87, 339
Ferrari, C. 2018, SSRv, 214, 111
Filacchione, G., Ciarniello, M., D'Aversa, E., et al. 2018, GeoRL, 45, 2184
Flasar, F. M., Kunde, V. G., Abbas, M. M., et al. 2004, SSRv, 115, 169
Hamilton, D. P., & Burns, J. A. 1994, Sci, 264, 550
Hanel, R., Conrath, B., Flasar, F. M., et al. 1981, Sci, 212, 192
Hanel, R., Crosby, D., Herath, L., et al. 1980, ApOpt, 19, 1391
Hansen, O. L. 1973, Icar, 18, 237
Hapke, B. 1993, Topics in Remote Sensing (Cambridge: Cambridge Univ. Press)
Howett, C.J.A., Spencer, J.R., Hurford, T., Verbiscer, A., & Segura, M. 2019, Icar, 321, 705

Howett, C. J. A., Spencer, J. R., Hurford, T., Verbiscer, A., & Segura, M. 2012, Icar, 221, 1084
Howett, C. J. A., Spencer, J. R., Hurford, T., Verbiscer, A., & Segura, M. 2014, Icar, 241, 239
Howett, C. J. A., Spencer, J. R., Hurford, T., Verbiscer, A., & Segura, M. 2016, Icar, 272, 140
Howett, A., Spencer, J. R., Nordheim, T. A., et al. 2020, Icar, 348, 113745
Howett, C. J. A., Spencer, J. R., Pearl, J., & Segura, M. 2010, Icar, 206, 573
Howett, C. J. A., Spencer, J. R., Schenk, P., et al. 2011, Icar, 216, 221
Juhász, A., & Horányi, M. 2015, AGUFM, P51B–2060
Kempf, S., Horányi, M., Hsu, H.-W., et al. 2018, in Enceladus and the Icy Moons of Saturn, ed. P. M. Schenk et al. (Tucson, AZ: Univ. Arizona Press), 195
Morrison, D., & Cruikshank, D. P. 1973, Icar, 18, 224
Nelder, J. A., & Mead, R. A. 1965, CompJ, 7, 308
Neugebauer, G., Matthews, K., Nicholson, P. D., et al. 2005, Icar, 177, 63
Nixon, C. A., Ansty, T. M., Lombardo, N. A., et al. 2019, ApJS, 244, 14
Nixon, C. A., Teanby, N. A., Calcutt, S. B., et al. 2009, ApOpt, 48, 1912
Nordheim, T. A., Hand, K. P., Paranicas, C., et al. 2017, Icar, 286, 56
Paranicas, C., Roussos, E., Decker, R. B., et al. 2014, Icar, 234, 155
Pearl, J. C., Kaelberer, M. S., Segura, M. E., Spencer, J. R., & Howett, C. 2008, BAAS, 40, 510
Pilinski, E. B., & Lee, A. Y. 2009, JSpRo, 46, 1007
Pitman, K. M., Buratti, B. J., & Mosher, J. A. 2010, Icar, 206, 537
Rathbun, J. A., Rodriguez, N. J., & Spencer, J. R. 2010, Icar, 210, 763
Schaible, M. J., Johnson, R. E., Zhigilei, L. V., & Piqueux, S. 2017, Icar, 285, 211
Schenk, P., Hamilton, D. P., Johnson, R. E., et al. 2011, Icar, 211, 740
Sciponi, F., Tosi, F., Stephan, K., et al. 2013, Icar, 226, 1331
Showalter, M. 1995, Saturn Viewer Help, https://pds-rings.seti.org/tools/viewer3_sat_help.shtml#VERSION3
Spencer, J. R. 1987, Icar, 69, 297
Spencer, J. R. 1989, Icar, 83, 27
Spencer, J. R. 1999, Sci, 284, 1514
Spencer, J. R., & Moore, J. 1992, Icar, 99, 261
Stephan, K., Jaumann, R., Wagner, R., et al. 2010, Icar, 206, 631
Verbiscer, A., French, R., Showalter, M., & Helfenstein, P. 2007, Sci, 315, 815
Young, L. A. 2017, Icar, 284, 443